

Chapter 5

SELF-ORGANIZATION OF SPATIAL SOLITONS

5.1. INTRODUCTION

In this chapter we present experimental results on the self-organization of spatial solitons in a self-focusing nonlinear medium. We have observed the emergence of order, self organization and a transition to a chaotic state. Nonlinear interactions between light and matter can lead to the formation of spatial patterns and self-trapped optical beams. Modulation instability is responsible for the spontaneous formation of optical patterns, which have been observed both with coherent and incoherent light [1,2]. Under certain conditions, self-trapped optical beams (spatial solitons) can be generated through the interplay between diffraction and nonlinear effects [3-5]. Self-trapped light filaments have been observed in materials with quadratic [6] and cubic [7] (Kerr) optical nonlinearities. Spatial solitons can interact through collisions [8,9], which opens the possibility of using them to perform computations [10]. Optical filaments can also act as waveguides, and it was recently shown that in liquid crystals they can be steered using an applied voltage [11]. Applications involving the use of spatial solitons will most likely require large numbers of them; however, the effects of the interactions between large numbers of filaments remain largely unexplored. Here we report the observation of self-organization of spatial solitons into a periodic array and the later breakdown of the periodicity. The array initially forms with a period that depends on the intensity of the illuminating beam. If the filaments are formed too closely they rearrange themselves into an array with a larger more stable period. This result has implications for the density with which solitons can be packed both for information processing and communication applications.

A light pulse propagating in a nonlinear Kerr medium will come to a focus if its power is above a critical value. If the pulse power is much higher than the critical power then the optical beam will break up into multiple filaments [12-14]. Each filament will contain approximately the critical power, defined as [15]:

$$P_{cr} = \frac{\pi(0.61)^2 \lambda^2}{8n_0 n_2}. \quad (5.1)$$

where λ is the laser wavelength in vacuum, n_0 is the linear refractive index of the material and n_2 is the material constant that gives the strength of the Kerr nonlinearity in units of inverse light intensity. We have used carbon disulfide as the nonlinear material ($n_0 = 1.6$, $n_2 = 3 \times 10^{-15} \text{ cm}^2/\text{W}$ [16]), which has a critical power of 190 kW for our laser wavelength of 800 nm.

5.2 EXPERIMENTAL SETUP

The experimental setup is shown in Figure 5.1. A Ti:Sapphire laser amplifier system is used to generate 150-femtosecond pulses with a maximum energy of 2 mJ. The standard deviation in laser pulse energy from shot-to-shot is 3%. The laser is run at the maximum energy level to achieve maximum stability, and neutral density filters are used to adjust the pulse energy in the experiment. Each pulse from the laser is split into pump and probe pulses. The pump pulse propagates through a 10 mm glass cell filled with carbon disulfide (CS_2). The beam profile of the pump at the exit of the glass cell is imaged onto a CCD camera (CCD 1) with a magnification factor of 5. A cylindrical lens (focal length = 10 cm) focuses the pump beam into a line approximately 3 mm inside the medium. The line focus generates a single column of filaments. We studied the filamentation process using Femtosecond Time-resolved Optical Polarigraphy (FTOP) [17]. This technique uses the transient birefringence induced in the material through the Kerr effect to capture the beam profile. The probe pulse propagates in a direction perpendicular to the pump. The presence of the pump induces a transient birefringence proportional to the intensity of the pulse. The

trajectory of the pump pulse can be captured with high temporal resolution by monitoring the probe pulse through cross polarizers. In our experimental setup (Fig. 5.1), the pump is polarized in the vertical direction and the probe is polarized at 45 degrees with respect to the pump's polarization. After the probe traverses the nonlinear medium it goes through an analyzer (polarizer at -45 degrees) and is imaged on a second CCD camera (CCD 2) with a magnification factor of 6. Light from the probe reaches the detector only if the probe temporally and spatially overlaps with the pump inside the nonlinear material. A delay line is used to synchronize the arrival of pump and probe pulses, and allows us to observe the pump at different positions along the direction of propagation.

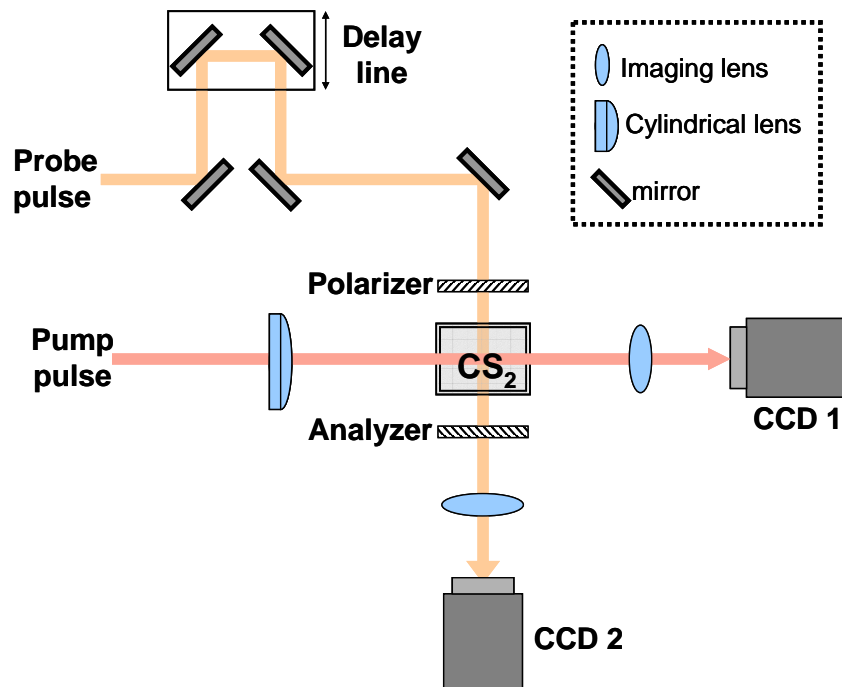


Figure 5.1. FTOP setup. The pump pulse is focused in the material with a cylindrical lens to generate a single column of filaments. The beam profile at the output is imaged on CCD 1. The probe pulse goes through a variable delay line, a polarizer and analyzer and is imaged on CCD.

5.3. EXPERIMENTAL RESULTS

5.3.1. Beam profile and instabilities as a function of pulse energy

Figure 5.2 shows the beam profile of the pump beam at the output of the CS₂ cell (CCD 1 in Fig. 1) as a function of pump pulse power. In the absence of nonlinearity the incident cylindrical beam would diverge to a width of 200 μm as it propagates to the output surface. For a pulse power equal to 12 times the critical power ($P = 12 P_{cr}$, Fig. 5.2a), self focusing and diffraction nearly balance each other, and the output beam width is approximately the same as for the input. For higher pulse power the beam self focuses into an increasingly thinner line (Figs. 5.2b and 5.2c) with a minimum width equal to 16 μm for $P = 80 P_{cr}$. It is clearly evident in Fig. 5.2c that modulation instability has generated self focusing in the orthogonal direction as well. For $P > 100 P_{cr}$, the beam breaks up into individual filaments (Fig. 5.2d-e). The filaments are seeded by small variations in the input beam and are stable in location and size to small variations in the input energy. In other words, the pattern of filaments is repeatable from shot to shot as long as the illuminating beam profile is kept constant. The diameter of the filaments is approximately 12 μm and does not change when the energy is increased, while the number of filaments increases with power. When $P > 250 P_{cr}$, the output beam profile becomes unrepeatable and the filaments start to fuse into a continuous line (Fig 2f-h). We will explain the origin of this instability later on. Part of the energy is scattered out of the central maximum into side lobes. The mechanism responsible for the formation of the side lobes is the emission of conical waves [18,19] during the formation of the filaments. The diameter of the filaments initially decreases until it reaches a stable condition; at this point some of the energy is released through conical emission while the rest of the energy is trapped in the filament [20].

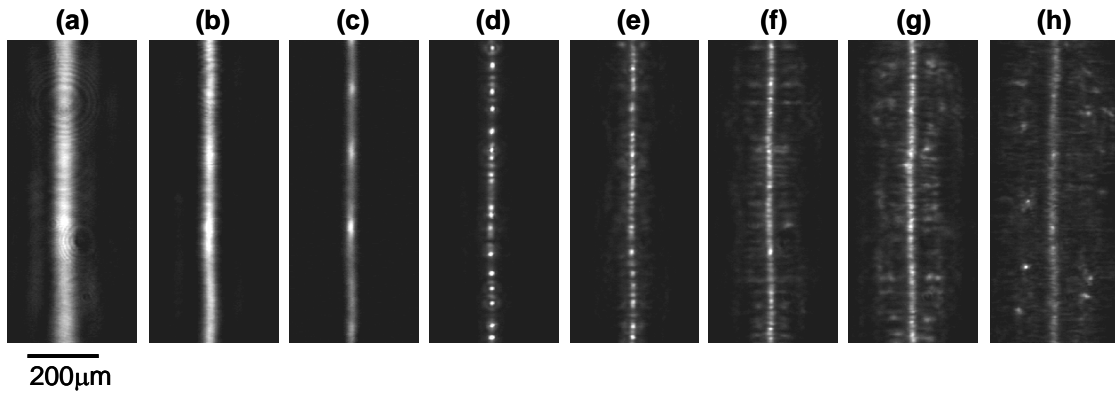
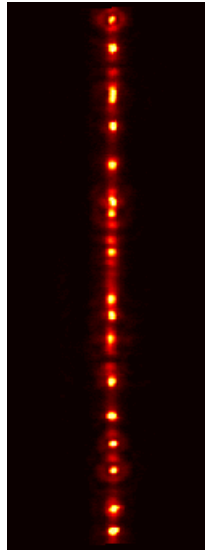
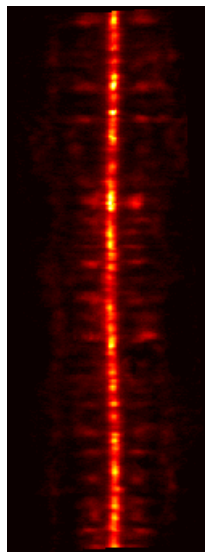


Figure 5.2. Beam profile of the pump pulse at the output of the CS₂ cell. The power increases from left to right: a) $P = 12P_{cr}$, b) $40P_{cr}$, c) $80P_{cr}$, d) $170P_{cr}$, e) $250P_{cr}$, f) $390P_{cr}$, g) $530P_{cr}$, h) $1200P_{cr}$. The size of each image is 0.36 mm (h) x 0.89 mm (v).

Video 5.1 and Video 5.2 show how the shot-to-shot fluctuations in the pulse energy affect the beam profile at the output of the cell. For each video, ten images were captured with the same experimental conditions and compiled into a movie clip, the only variable being the fluctuations in the laser pulse energy. For a pulse with a power of $170 P_{cr}$ the output beam profile is stable (Video 5.1). There are only small changes in the position of the filaments while the overall pattern of filaments remains constant. Filaments that appear close to each other seem to be the most sensitive to the energy fluctuations. If the power is increased to $390 P_{cr}$ the beam profile at the output becomes unrepeatable (Video 5.2). The position of the filaments varies greatly from shot to shot and the central line bends differently for each shot.



Video 5.1. Movie of changes in the beam profile as a result of fluctuations in the pulse energy for $P = 170 P_{cr}$ (78.5 KB). The image area is 0.36 mm (h) x 0.89 mm (v).



Video 5.2. Movie of changes in the beam profile as a result of fluctuations in the pulse energy for $P = 390 P_{cr}$ (113 KB). The image area is 0.36 mm (h) x 0.89 mm (v).

Increasing the pulse energy causes the beam to self-focus faster and break up into filaments earlier. As shown above, further increasing the energy causes the beam to become unstable. For low energy levels the beam profile remains uniform, but as the energy is increased the beam breaks up into a periodic array of filaments. We have measured the beam profile at a fixed distance from the cell entrance for eight different pulse energies. The beam profile is captured using the FTOP setup with a fixed delay. Figure 5.3a shows a cross section of the beam profile at a distance of 2.5 mm inside the cell for pulse power of $P = 250 P_{cr}$, $390 P_{cr}$, $530 P_{cr}$, $790 P_{cr}$, $1200 P_{cr}$, $1700 P_{cr}$, $2700 P_{cr}$, $3800 P_{cr}$. Higher power levels are necessary to observe filaments after a distance of 2.5 mm, as opposed to 10 mm in Figure 5.2. Figure 5.3b shows the Fourier transform of the beam cross sections in Figure 5.3a. The central peak (DC component) in the Fourier transform is blocked to visualize the secondary peaks. For $P = 250 P_{cr}$, no filaments are observed as the beam remains uniform after 2.5 mm. Note that for this power the beam completely breaks up into filaments after 10 mm (Fig. 5.2e). As the power is increased between $390 P_{cr}$ and $790 P_{cr}$ an increasing number of filaments appears in a periodic array. The periodicity is clearly visible in the Fourier transform; a peak appears that corresponds to the spacing between the filaments ($\sim 20 \mu\text{m}$). The emergence of periodicity in the beam pattern is discussed in the following section. When the power is increased above $1200 P_{cr}$ the periodicity starts to disappear. The beam is no longer uniform but there is no clear indication of the formation of filaments. This state corresponds to the patterns in Figure 2f-h, where the beam profile becomes unstable.

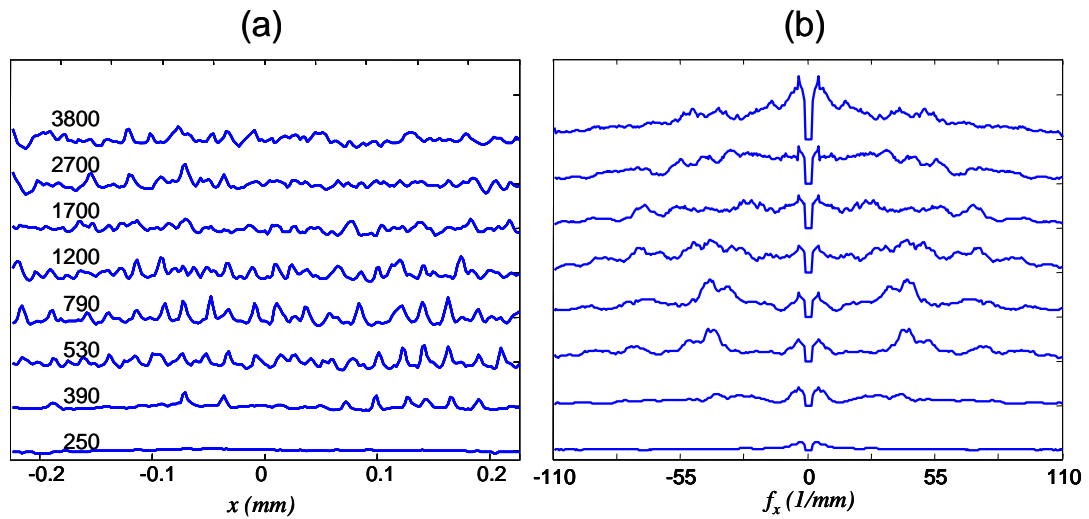


Figure 5.3. Beam profile inside the cell as a function of power. (a) Cross sections of the beam profile at 2.5 mm inside the cell for pulse power $P/P_{cr} = 250, 390, 530, 790, 1200, 1700, 2700, 3800$. The cross sectional plots for different powers are displaced vertically for visual clarity. The lowest power is displaced at the bottom. The peaks correspond to regions of higher intensity (filaments). (b) Fourier transform of the plots in (a). The peaks represent the periodicity of the arrays of filaments. A strong central peak (DC component) is zeroed to display the secondary peaks.

5.3.2. Spatial evolution of the beam and self-organization

Video 5.3 shows the filamentation process for a pulse with $P = 390 P_{cr}$. The pulse propagation inside the material is captured from 2 mm to 4 mm from the cell entrance using the FTOP setup. The width of the image of the pulse on the CCD camera (CCD 2 in Fig. 5.1) depends on the pulse duration and the time response of the material. CS_2 has both a very fast (femtosecond) electronic time response and a slower (picosecond) molecular response. In our experiments, the time response at the leading edge of the signal is essentially instantaneous, and the resolution is determined by the pulse duration (150

femtoseconds). On the trailing edge of the signal a slower decay time of approximately 1.5 picoseconds is observed, which is consistent with the time constant for the molecular response of the material. The movie clip in Video 3 shows the propagation of a pulse with a spatial profile that is initially uniform. The movie is compiled from multiple pump-probe experiments by varying the delay of the probe pulse. As the beam propagates the intensity modulation increases until the beam breaks up into filaments. The light is trapped in the filaments, which continue to propagate with a constant diameter for several millimeters.



Video 5.3. Pulse propagation inside CS_2 from 2 mm to 4 mm from the cell entrance for a pulse power of $390 P_{cr}$. An initially uniform beam breaks up into stable filaments (258 KB). The image size is 2.4 mm (h) x 1.6 mm (v).

Figure 5.4 shows the trajectory of the beam obtained in the FTOP setup for pulses with $P = 390 P_{cr}$ (a) and $1200 P_{cr}$ (c), from a distance of 0.5 cm to 5 cm from the cell entrance. The trajectory is obtained by numerically combining multiple pump-probe images of the pulse at different positions as it traverses the material. The 1-D Fourier transforms of the beam profile are calculated and displayed in Figure 5.4b and 5.4d for each position along the propagation direction. The peaks in the Fourier transform correspond to the periodicity in the positions of the filaments. The central peak (DC component) in the Fourier transform is

blocked to improve the contrast in the image. Periodic changes in the amplitude of the peaks along the propagation direction are artifacts due to the sampling of the beam profile in the experiments.

The pulse with lower power (Fig. 5.4a) breaks up into filaments at a distance of 2.9 mm into the material, while the pulse with higher power (Fig. 5.4c) breaks up at 1.5 mm from the cell entrance. The Fourier transform in Fig. 4b clearly shows how a periodicity emerges during the filamentation process. The filaments are created in a regular array and propagate undisturbed for several millimetres. The spacing between the filaments is approximately 40 μm , about four times the diameter of the filaments. If the pulse energy is higher (Fig. 5.4d) the array of filaments initially forms with a higher spatial frequency. The period then increases from 22 μm to 33 μm as the filaments propagate. After 5 mm the sharp peaks visible in the Fourier transform start to fan out. The gradual loss of the periodicity after 5 mm corresponds to a decline in the number of filaments. We attribute the change in the period of the soliton array primarily to the interactions between nearby filaments. These interactions cause filament fusion and conical emission, redirecting some of the energy away from the main line of solitons. The filaments then continuously rearrange themselves in a sparser grid. The interactions depend on the relative phase of the filaments. Filaments of the same phase will attract while out-of-phase neighboring filaments will repel. The phase of individual filaments is determined by the initial condition (the illuminating beam) but also by the accumulated phase along the propagation path with linear and nonlinear contributions. Slight intensity or angle changes can lead to large accumulated phase differences. We believe that this effect is responsible for the onset of the chaotic behaviour we observe.

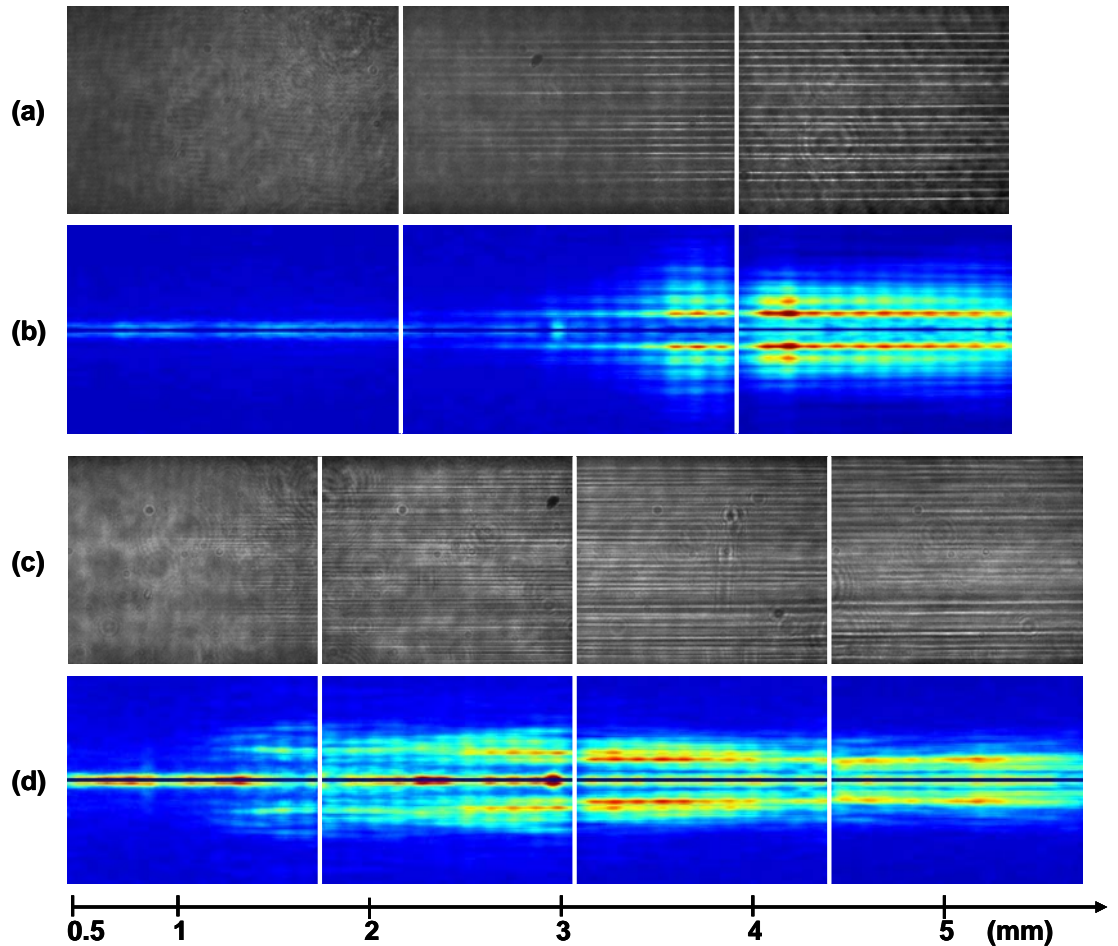


Figure 5.4. Pulse trajectories and 1-D Fourier transforms. (a,c) The trajectory of the pulse is reconstructed by digitally adding up the FTOP frames for different positions of the pulse. Each separate image corresponds to frames taken for a fixed position of CCD camera. The camera was moved laterally to capture the beam profile farther along inside the cell. The pulse power is $390P_{cr}$ in (a) and $1200P_{cr}$ in (c). (b,d) Show the 1-D Fourier transforms of the filamentation patterns in (a) and (c), respectively. The central component is blocked to visualize higher frequencies.

Figure 5.5 shows the cross sectional plots of the filament formation for the pulse with $P = 390 P_{cr}$. The figure shows the beam profile for 6 different positions inside the material during the filament formation phase. The propagation distance increases from bottom to top (the plots are separated for visual clarity) with an increment of $250 \mu\text{m}$ for each plot. The first cross section (Fig. 5.5a) shows a uniform beam profile, at a distance of 2.4 mm from the entrance of the cell. In the second there is some redistribution of the intensity into local maxima, with peaks of approximately $30 \mu\text{m}$ in diameter (Fig. 5.5b). The peaks continue to grow until they reach a diameter of about $10 \mu\text{m}$ and become stable. The whole process of filamentation happens in just over 1 mm of propagation (Fig. 5.5b-f).

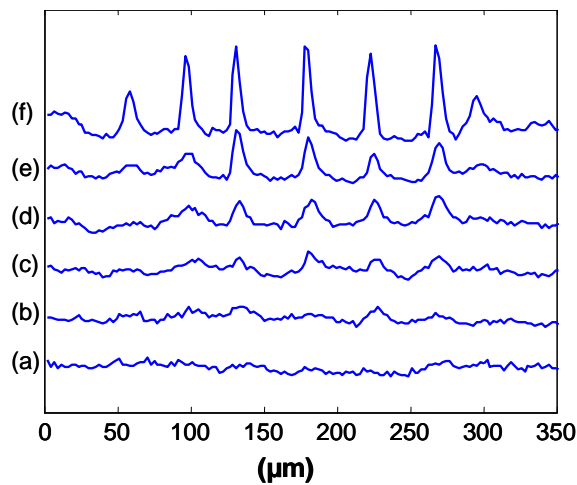


Figure 5.5. Cross sectional plots of filament formation for $P = 390 P_{cr}$. Each plot represents a fraction of the beam profile (0.35 mm) at a specific distance from the cell entrance: 2.40 mm (a), 2.65 mm (b), 2.90 mm (c), 3.15 mm (d), 3.40 mm (e) and 3.65 mm (f).

Figure 5.6 shows a close-up of filament interactions from 3.5 mm to 4.2 mm inside the material for $P = 1200 P_{cr}$. Regions (a) and (c) show stable filaments that propagate through undisturbed. Region (b) of Fig. 5.6 shows two filaments merging. This interaction is similar to the attraction force experienced by solitons in close proximity. The filaments start out

separated by $20\ \mu\text{m}$, and only one filament is seen to survive after the interaction. Region (d) shows a filament that starts out with a small diameter and diverges. The filament size continues to increase until it overlaps with a neighbor, after which a single filament continues to propagate (not shown in the picture). In region (e) a new filament is formed well inside the material. It is not clear whether the new filament is generated by the background light or if it splits from an existing filament. As the pulse continues to propagate the number of filaments continues to decrease, until the output at 10 mm where we see almost a continuous line at the center with only a few distinguishable filaments (Fig. 5.2h).

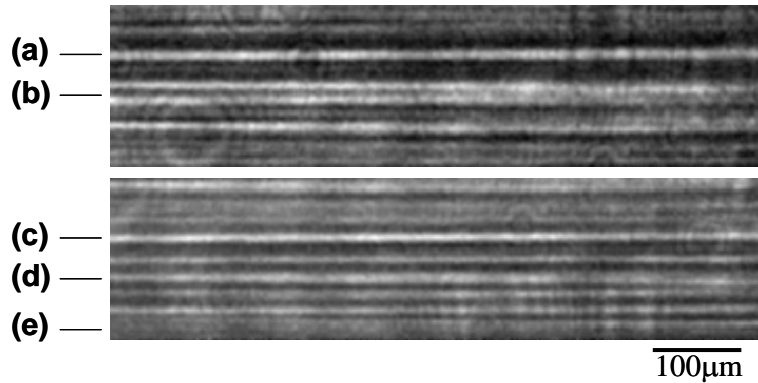


Figure 5.6. Interactions between filaments from 3.5 mm to 4.2 mm from the cell entrance for an input pulse power of $1200 P_{cr}$. Some filaments propagate undisturbed (a-c). We have observed fusion of two filaments (b), divergence of a filament (d) and the generation of a new filament (e).

5.3.3. Periodic arrays of filaments

A stable array of filaments can be launched by modulating the input beam. If the separation between the filaments is large enough the filaments will not interact. Figure 5.7 shows the propagation of filaments generated by placing an amplitude grating ($40\ \mu\text{m}$ period) before

the entrance of the cell. The input power is $P = 200 P_{cr}$. Filaments form very quickly and propagate undisturbed (Fig. 5.7a). The 1-D Fourier transform in Fig. 5.7b shows that the period induced by the grating does not change with propagation. Figure 5.7c shows the array of filaments at the output face of the cell (10mm propagation). The propagation distance of the filaments in this case is limited by the cell length. The modulation of the beam amplitude speeds up the formation of the filaments, while the input energy ensures the stability. Most of the available energy is trapped in the filaments; no light was detected outside of the filaments. The energy in each filament can be estimated from the total energy and the number of filaments. Each filament carries approximately four times the critical power ($4 P_{cr}$).

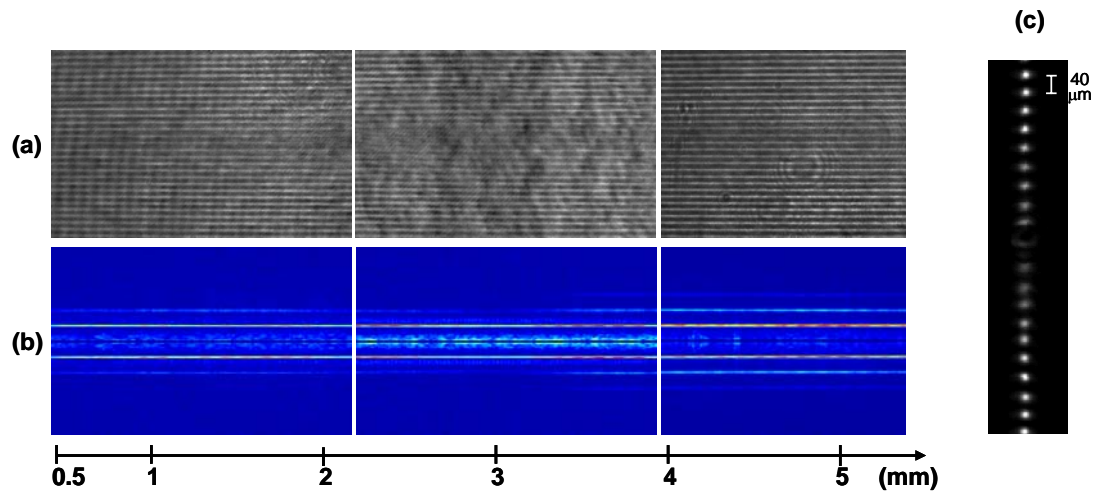


Figure 5.7. Propagation of a pulse with a periodic beam profile (a) The trajectory of the pulse is reconstructed by digitally adding up the FTOP frames for different positions of the pulse. (b) 1-D Fourier transforms of the filamentation patterns in (a). The central component is blocked to visualize higher frequencies. (c) Image of the beam profile at the output of the cell after 10 mm of nonlinear propagation.

We have also generated 2-D arrays of filaments. The cylindrical lens is removed from the setup for this experiment, so the input intensity is decreased. The input beam (5 mm

FWHM) is modulated using an amplitude mask at a distance of 10 cm from the cell. The mask is a chessboard pattern with a period of 128 μm . The diffraction pattern incident on the cell has a periodic modulation that seeds the formation of filaments in a periodic 2-D array. Figure 5.8 shows the beam at the output of the cell for different pulse energies. The pictures show only a fraction of the beam profile (0.96 mm x 1.28 mm). Figure 8a shows the beam profile for a low energy where the nonlinearities are weak. The periodic modulation is due to the mask. As the power is increased filaments start to form at the local maxima of the intensity profile. For the maximum power all of the local maxima self-focus into filaments, thus creating a 2-D array of filaments.

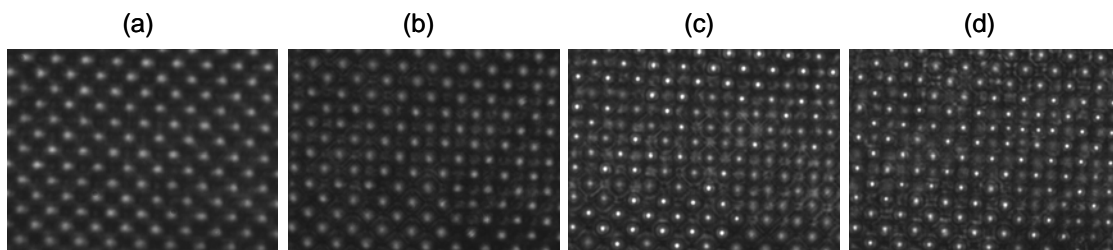


Figure 5.8. Formation of a 2-D array of filaments. More filaments appear as the pulse energy is increased: (a) 0.01 mJ, (b) 0.46 mJ, (c) 0.71 mJ, (d) 1.0 mJ. The area of each image is 1.28 mm x 0.96 mm.

5.4. NUMERICAL SIMULATIONS

The experimental results were verified using a numerical simulation. The propagation model is a time-averaged nonlinear Schrodinger equation that includes the effects of diffraction, third order nonlinearity (Kerr effect) and two-photon absorption [21]. A fifth order nonlinearity was also included to account for the stability of the filaments observed experimentally. The negative index change generated through the fifth order nonlinearity

balances the positive Kerr index change. A complete simulation of the spatial and temporal profile of the nonlinear pulse propagation requires very fine sampling in three spatial dimensions and time. We assume in our model that the temporal profile of the pulse is constant, which allows us to calculate the beam evolution with good spatial resolution. We have shown in Chapter 4 that this model provides a good approximation to the propagation of femtosecond pulses in CS₂. The light propagation is calculated assuming a scalar envelope for the electric field, which is slowly varying along the propagation direction z . The evolution of the scalar envelope is given by the equation:

$$\frac{dA}{dz} = \frac{i}{2kn_0} \left(\frac{\partial^2}{\partial x^2} + \frac{\partial^2}{\partial y^2} \right) A + ik(n_2|A|^2)A - ik(n_4|A|^4)A - \beta|A|^2 A \quad (5.2)$$

$A(x,y,z,T)$ is the complex envelope of the electric field, $k = \frac{2\pi}{\lambda}$, $\lambda = 800\text{nm}$, $n_0 = 1.6$, $n_2 = 3 \times 10^{-15} \text{cm}^2/\text{W}$ [16], $n_4 = -2 \times 10^{-27} \text{cm}^4/\text{W}^2$, $\beta = 4.5 \times 10^{-13} \text{cm}/\text{W}$ [21]. The first term on the right-hand side accounts for diffraction, the second is Kerr self-focusing (third-order nonlinearity), the third term accounts for the fifth-order nonlinearity and the last term represents for two-photon absorption. Linear absorption is negligible at the wavelength used in the experiments. The equation is solved numerically using the Split-step Fourier method.

The two-photon absorption term affects the propagation only for the highest intensity levels and does not significantly change the qualitative behaviour observed in the simulations. The fifth-order nonlinearity (n_4) is the mechanism responsible for the generation of stable light filaments. Since we could not find experimentally measured values of n_4 , in the simulation we have assigned it the value that gave the best match with the experimental results. The stabilization of the filaments can also be caused by a negative index change due to the plasma generation. If the light intensity is high enough a plasma can be created through multiphoton absorption. However, the intensity of the filaments is well below the threshold for plasma generation [20]; therefore multiphoton ionization does not play a significant role in the filament dynamics and does not need to be included in the simulations.

The input beam for the simulation is generated using the image of the beam in Fig. 5.2a. The square root of the measured intensity profile is used as the amplitude of the input light field, and a phase profile is added to simulate the phase of the focused beam at the entrance of the cell. The simulated field is a good approximation to the experimental input beam and has a similar noise profile.

The model in equation 5.2 was used to numerically calculate the output beam profile after propagating through 10 mm of CS₂. Figure 5.9 shows a comparison of the numerical and experimental results. The simulation follows the experimental results very closely during the self-focusing stage (Fig. 5.9a-c). The beam self-focuses into a line of decreasing width as the power is increased. There is also good agreement between simulation and experiment when the beam breaks up into filaments (Fig. 5.9d-e). The number of filaments is similar, and in both cases the filaments release some energy through conical emissions. The difference in the spacing of the filaments is discussed below. Up to this point the behaviour observed in the simulation is very similar to the experiments; however, the simulation does not capture the behaviour of the beam in the chaotic stage (Fig. 5.9f-h). In the experiments some energy is lost and the filaments disappear. A central bright line remains and is surrounded by side-lobes that propagate away from the center. For the highest power level new filaments appear in the side-lobes. The simulation shows different behaviour, as more filaments appear in the central line and then start moving away. In the numerical results the array becomes unstable as the density of the filaments increases and some of the filaments get deflected through their mutual interactions; however, only some of the filaments disappear while a lot of them survive. In fact, in the simulations most of the energy is trapped in the filaments, even for the highest power levels.

The loss seems to be a key element in the discrepancy between experiment and simulation. The only source of loss in the simulation is two-photon absorption, which does not dissipate enough energy when compared to the experiment. It is not clear what causes the energy loss in the experiments. Another source of error is in the temporal domain that is neglected in the simulations. The spectral content of the solitons increases as they propagate, which is ignored in the simulation. It is possible that the energy that is

transformed to higher frequencies is no longer trapped in the soliton. A full 3-D simulation might help in resolving some of these issues.

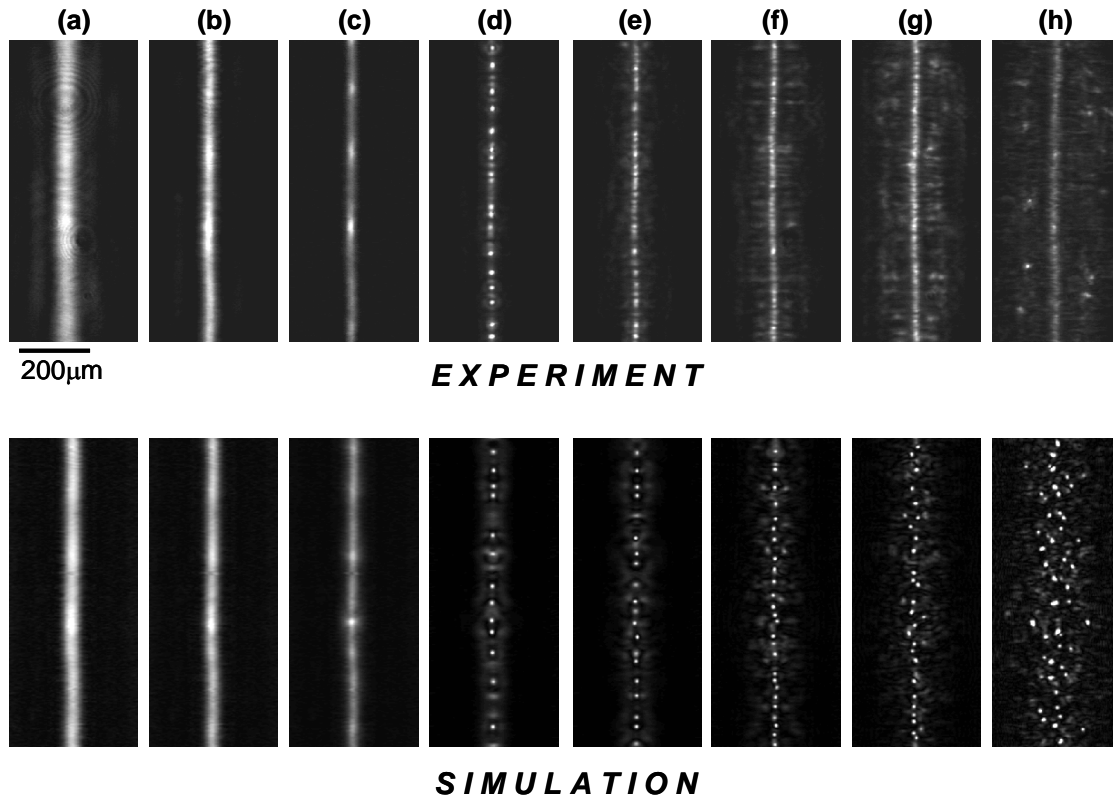


Figure 5.9. Comparison of experimental and numerical results of beam profile as a function of pulse energy. The power increases from left to right: a) $P = 12 P_{cr}$, b) $40 P_{cr}$, c) $80 P_{cr}$, d) $170 P_{cr}$, e) $250 P_{cr}$, f) $390 P_{cr}$, g) $530 P_{cr}$, h) $1200 P_{cr}$.

The beam profile as viewed from the side was also calculated for a propagation distance of 10 mm. Figure 10 shows the 1-D Fourier transforms of the beam profile for four different power levels, $250 P_{cr}$, $390 P_{cr}$, $530 P_{cr}$ and $1200 P_{cr}$. In Fig. 5.10a we can clearly see that after a propagation distance of 6 mm the filaments form a periodic array (with a period of approximately $30 \mu\text{m}$), which remains constant for several millimeters and starts to break down only towards the end of the cell. Fig. 5.10b shows a periodic arrangement that starts

with a slightly smaller period before settling to a period of $30\ \mu\text{m}$. For the input power in Fig. 5.10c the filaments initially form with a period of $16\ \mu\text{m}$ after a propagation distance of $3\ \text{mm}$. As the light propagates to a distance of $6\ \text{mm}$ the period increases to $25\ \mu\text{m}$, and after this point the period seems to continue to increase but the peaks in the Fourier transform start to fan out as the array of filament loses its periodicity. For the highest energy level (Fig. 5.10d) multiple peaks appear in the Fourier transform, with a trend towards smaller spatial frequencies with increasing propagation distance. At this level no clear periodicity is observed in the simulations. The behavior observed in the simulations is very similar to that of the experimental results. In both cases order (periodicity) emerges, evolves and eventually dissipates. In the simulations the filaments form with a smaller period and the filamentation distance is longer. We attribute these differences to the lack of knowledge of the exact initial conditions (beam intensity and phase), approximations made in the numerical model and uncertainties in the constants used for the simulation.

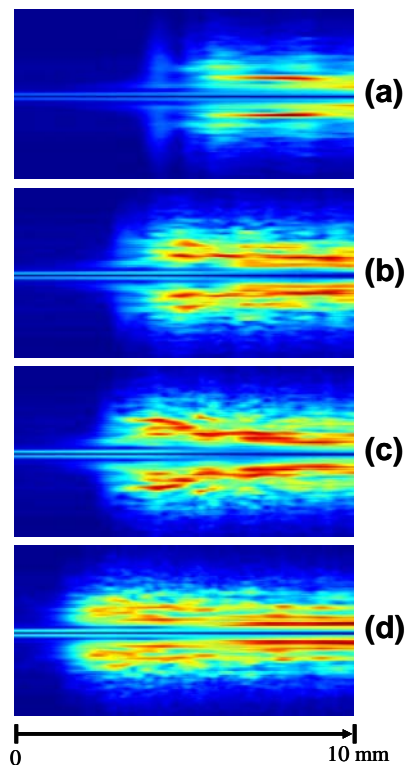


Figure 5.10. 1-D Fourier transforms for numerically calculated beam propagation.

The beam propagation is numerically calculated for four different power levels a) $P =$

250 Pcr, b) 390 Pcr, c) 530 Pcr, d) 1200 Pcr. A 1-D Fourier transform on the side view of the beam profile is calculated for each along the propagation direction. The total distance is 10 mm. The central peak (DC component) in the Fourier transform is blocked to improve the contrast in the image.

5.5. SUMMARY

We have observed the emergence of order, self organization and a transition to a chaotic state in an optical self-focusing nonlinear medium. Order emerges through the formation of spatial solitons in a periodic array. If the initial period of the array is unstable the solitons will tend to self-organize into a larger (more stable) period. These results provide new insight into the collective behaviour of solitons in nonlinear systems and will impact potential applications using arrays of solitons for computation or communications. A time-averaged nonlinear Schrodinger equation was used to model the propagation numerically. The numerical simulations were in good agreement with the experiments and captured the formation of filaments and self-organization, but did not reproduce the beam instabilities for the highest power levels observed experimentally.

REFERENCES

- [1] M. Saffman, G. McCarthy, W. Krolikowski, *J. Opt. B.* **6**, 387-403 (2004).
- [2] D. Kip, M. Soljacic, M. Segev, E. Eugenieva, D. N. Christodoulides, *Science* **290**, 495-498 (2000).
- [3] G. I. Stegeman, M. Segev, *Science* **286**, 1518-1523 (1999).
- [4] A. Barthelemy, S. Maneuf, C. Froehly, *Opt. Comm.* **55**, 201-206 (1985).
- [5] M. Segev, B. Crosignani, A. Yariv and B. Fischer, *Phys. Rev. Lett.* **68**, 923-926 (1992).
- [6] W. E. Torruelas, Z. Wang, D. J. Hagan, E. W. Vanstryland, G. I. Stegeman, L. Torner, C. R. Menyuk, *Phys. Rev. Lett.* **74**, 5036-5039 (1995).
- [7] A. J. Campillo, S. L. Shapiro, and B. R. Suydam, *Appl. Phys. Lett.* **23**, 628-630 (1973).
- [8] J. P. Gordon, *Opt. Lett.* **8**, 596-598 (1983).
- [9] M. Shalaby, F. Reynaud, and A. Barthelemy, *Opt. Lett.* **17**, 778-780 (1992).
- [10]. R. Mcleod, K. Wagner, and S. Blair, *Phys. Rev. A* **52**, 3254-3278 (1995).
- [11] M. Peccianti, C. Conti, G. Assanto, A. De Luca, C. Umeton, *Nature* **432**, 733 (2004).
- [12] M. Mlejnek, M. Kolesik, J. V. Moloney, and E. M. Wright, *Phys. Rev. Lett.* **83**, 2938-2941 (1999).
- [13] L. Berge, S. Skupin, F. Lederer, G. Mejean, J. Yu, J. Kasparian, E. Salmon, J. P. Wolf, M. Rodriguez, L. Woste, R. Bourayou, R. Sauerbrey, *Phys. Rev. Lett.* **92**, 225002 (2004).
- [14] H. Schroeder and S. L. Chin, *Opt. Comm.* **234**, 399-406 (2004).
- [15] R Boyd, *Nonlinear Optics*, Academic Press, 2003.

- [16] R. A. Ganeev, A. I. Ryasnyansky, M. Baba, M. Suzuki, N. Ishizawa, M. Turu, S. Sakakibara, H. Kuroda, *Appl. Phys. B* **78**, 433-438 (2004).
- [17] M. Fujimoto, S. Aoshima, M. Hosoda, and Y. Tsuchiya, *Opt. Lett.* **24**, 850-852 (1999).
- [18] G. G. Luther, A. C. Newell, and J. V. Moloney, E. M. Wright, *Opt. Lett.* **19**, 789-791 (1994).
- [19] E. T. J. Nibbering, P. F. Curley, G. Grillon, B. S. Prade, M. A. Franco, F. Salin, and A. Mysyrowicz, *Opt. Lett.* **21**, 62-64 (1996).
- [20] M. Centurion, Y. Pu, M. Tsang, D. Psaltis, submitted to *Phys. Rev. A* (2005).
- [21] M. Falconieri, G. Salvetti, *Appl. Phys. B* **69**, 133-136 (1999).